RESEARCH ARTICLE

# Finite element analysis of trabecular bone microstructure using CT imaging and continuum mechanical modeling

Indranil Guha[1] | Xiaoliu Zhang[1] | Chamith S. Rajapakse[2] | Gregory Chang[3] | Punam K. Saha[1,4]

[1]Department of Electrical and Computer Engineering, College of Engineering, University of Iowa, Iowa City, Iowa, USA

[2]Departments of Radiology and Orthopaedic Surgery, University of Pennsylvania, Philadelphia, Pennsylvania, USA

[3]Department of Radiology, New York University Grossman School of Medicine, New York, New York, USA

[4]Department of Radiology, Carver College of Medicine, University of Iowa, Iowa City, Iowa, USA

**Correspondence**
Punam K. Saha, 4312 Seamans Center for the Engineering Arts and Sciences, Iowa City, IA 52242, USA.
Email: pksaha@healthcare.uiowa.edu

**Funding information**
NIH, Grant/Award Number: R01 HL142042

## Abstract

**Purpose:** Osteoporosis is a bone disease associated with enhanced bone loss, microstructural degeneration, and fracture-risk. Finite element (FE) modeling is used to estimate trabecular bone (Tb) modulus from high-resolution three-dimensional (3-D) imaging modalities including micro-computed tomography (CT), magnetic resonance imaging (MRI), and high-resolution peripheral quantitative CT (HR-pQCT). This paper validates an application of voxel-based continuum finite element analysis (FEA) to predict Tb modulus from clinical CT imaging under a condition similar to in vivo imaging by comparing with measures derived by micro-CT and experimental approaches.

**Method:** Voxel-based continuum FEA methods for CT imaging were implemented using linear and nonlinear models and applied on distal tibial scans under a condition similar to in vivo imaging. First, tibial axis in a CT scan was aligned with the coordinate $z$-axis at 150 $\mu$m isotropic voxels. FEA was applied on an upright cylindrical volume of interests (VOI) with its axis coinciding with the tibial bone axis. Voxel volume, edge, and vertex elements and their connectivity were defined as per the isotropic image grid. A calibration phantom was used to calibrate CT numbers in Hounsfield unit to bone mineral density (BMD) values, which was then converted into calcium hydroxyapatite (CHA) density. Mechanical properties at each voxel volume element was defined using its ash-density defined on CT-derived CHA density. For FEA, the bottom surface of the cylindrical VOI was fixed and a constant displacement was applied along the $z$-direction at each vertex element on the top surface to simulate a physical axial compressive loading condition. Finally, a Poisson's ratio of 0.3 was applied, and Tb modulus (MPa) was computed as the ratio of average von Mises stress (MPa) of volume elements on the top surface and the applied displacement. FEA parameters including mesh element size, substep number, and different tolerance values were optimized.

**Results:** CT-derived Tb modulus values using continuum FEA showed high linear correlation with the micro-CT-derived reference values ($r \in [0.87\ 0.90]$) as well as experimentally measured values ($r \in [0.80\ 0.87]$). Linear correlation of computed modulus with their reference values using continuum FEA with linear modeling was comparable with that obtained by nonlinear modeling. Nonlinear continuum FEA-based modulus values (mean of 1087.2 MPa) showed greater difference from their reference values (mean of 1498.9 MPa using micro-CT-based FEA) as compared with linear continuum methods. High repeat CT scan

reproducibility (intra-class correlation [ICC] = 0.98) was observed for computed modulus values using both linear and nonlinear continuum FEA. It was observed that high stress regions coincide with Tb microstructure as fuzzily characterized by BMD values. Distributions of von Mises stress over Tb microstructure and marrow regions were significantly different ($p < 10^{-8}$).

**Conclusion:** Voxel-based continuum FEA offers surrogate measures of Tb modulus from CT imaging under a condition similar to in vivo imaging that alleviates the need for segmentation of Tb and marrow regions, while accounting for bone distribution at the microstructural level. This relaxation of binary segmentation will extend the scope of FEA application to assess mechanical properties of bone microstructure at relatively low-resolution imaging.

# 1 | INTRODUCTION

Osteoporosis is an age-related bone disease characterized with reduced bone mineral density (BMD) and increased fragility and fracture-risk.[1,2] Nearly, one in four men and one in two women suffer one or more fragility fractures in their lifetime.[3] Dual-energy X-ray absorptiometry (DXA) computed BMD is clinically used to detect osteoporosis. It is known that BMD explains 60%–70% of the bone's mechanical competence and the remaining is contributed by several other factors such as trabecular bone (Tb) strength and microstructural basis.[4–7]

Finite element (FE) analysis (FEA) is widely used to compute Tb mechanical properties from high-resolution three-dimensional (3-D) images.[8–13] It has been shown that Tb modulus measures computed from FEA on micro-CT scans highly correlate with experimentally observed values, and often, micro-CT-based FEA is considered a gold-standard method for estimating Tb mechanical properties.[9–11,14] HR-pQCT- and MRI-based FEA have been validated and adopted for in vivo assessment of Tb mechanical properties in several studies.[8,15–19]

Whole-body CT imaging with emerging scanners has recently drawn interest as a viable modality for quantitative bone microstructural imaging at peripheral sites.[20] Major advantages of modern CT scanners include wide availability in clinical environments, ultra-high speed scanning, ultra-low dose radiation, large scan-length, and access at central skeletal sites. However, the application of FEA in CT imaging for the assessment of mechanical properties at the level of Tb microstructure is not well established. A major challenge with FEA of Tb microstructure from CT imaging is related to limited spatial resolutions, which often adds artifactual breaks and degenerated connectivity along segmented Tb microstructure. For example, the true

resolution at 10% modulation transfer function (MTF), available within the state-of-the-art CT scanners, is comparable to human Tb thickness.[20] Several methods have adopted BMD-adjusted continuum FEA on CT imaging.[21,22] However, these methods were not aimed to compute mechanical properties at the scale of bone microstructure, and these methods have been applied mostly at central sites, particularly at the hip. Bauer et al.[23] applied voxel-based continuum FEA using ex vitro CT imaging of small Tb specimens from thoracic vertebrae stored in a formalin solution after degassing. Their experimental results showed that the values of the failure load measure obtained by continuum FE modeling without thresholding bone and marrow regions are weakly correlated ($r < 0.63$) with experimental values.

In this paper, we examine the role of voxel-based continuum FEA using both linear and nonlinear modeling of material properties to assess Tb Young's modulus or simply modulus from clinical CT imaging under a condition similar to in vivo imaging without thresholding bone and marrow regions. Specifically, we use CT imaging of intact ankle specimens to simulate an in vivo imaging condition and examine the performance of voxel-based continuum FEA to predict Tb modulus measures derived from micro-CT and experimental approaches. Also, repeat scan reproducibility of CT-based continuum FEA is examined. Voxel-based continuum FEA alleviates the need for segmentation of Tb microstructure from surrounding marrow space, while accounting for bone distribution at the microstructural level. Tb modulus, examined in this paper, characterizes the resistance of bone microstructure to deformation and indicates an important measure of mechanical quality of Tb microstructure.[24,25] Also, it has been previously demonstrated that modulus highly correlates with yield strength and ultimate strength for both cortical and trabecular bone.[26] Thus, FEA-derived

Tb modulus measure will be useful in bone-related studies.

## 2 | METHODOLOGY

In this section, we describe our methods and experimental plans for CT-based FE modeling and modulus computation of Tb network without requiring explicit segmentation of the bone microstructure. Toward this goal, the following materials and methods were used— (1) cadaveric ankle specimens, (2) CT imaging, (3) micro-CT imaging, (4) mechanical testing, (5) image pre-processing, (6) voxel-based continuum FE analysis, and (7) experiments and data analysis.

## 2.1 | Cadaveric ankle specimens

Twenty-four fresh-frozen cadaveric ankle specimens were collected from 17 body donors (age (mean(std)): 79.6(13.2) year; nine females) under the Deeded Bodies Program at The University of Iowa, Iowa City, Iowa. Donors with knowledge of previous bone tumor, metastasis, or fracture at tibia were excluded. These specimens were separated at mid-tibia and soft tissues as well as the ankle joint and foot were preserved. The specimens were kept frozen in sealed plastic bags until CT imaging and were thawed at room temperature before scanning.

## 2.2 | CT imaging

All cadaveric specimens were scanned in vitro on a 128 slice SOMATOM Definition Flash scanner (Siemens, Forchheim, Germany) at the University of Iowa Comprehensive Lung Imaging Centre. Scan length of 10 cm beginning at the distal tibia end-plateau was selected, and the scans were acquired in single-tube spiral acquisition mode using the following parameters — 120 kV, 200 mA effective, 1 s rotation speed, pitch factor: 1.0, detector rows: 16, scan time: 23.2 s, collimation: 16 × 0.6 mm, total effective dose equivalent: 170 $\mu$Sv ≈ 20 days of environmental radiation in the United States. Siemens z-UHR scan mode was applied enabling Siemens dual $z$ sampling technology, which splits the signal on 0.6 mm detectors delivering 0.3 mm effective spatial resolution in the $z$-direction.[20] Images were reconstructed at 300 $\mu$m thickness and 200 $\mu$m slice-spacing using a normal cone beam method with a special U70 u kernel achieving high spatial resolution. Three CT scans were collected for each specimen after repositioning the specimen on the scanner table between each repeat scan. Ankle specimens were positioned using scanner-provided laser beam reference as described by Zhang et al.[27]

## 2.3 | Micro-CT imaging

Thirteen cadaveric specimens were scanned on a Micro-cat II (Siemens Pre-Clinical, Tennessee, USA) cone beam micro-CT scanner. Before micro-CT scans, soft tissues were removed from each specimen, and the tibia was dislodged from the ankle joint to fit into the scanner. Micro-CT scans were acquired in micro-focus mode with less than 6 $\mu$m focal spot generating a maximum resolution of 15 $\mu$m at 10% MTF. The following parameters were used—100 kV, 200 mAs, 720 projections over 220°, exposure of 1 s per projection, scan time: 12 min, 2 mm Al filter for beam hardening; scan-length: 29.5 mm; FOV on the $xy$ plane: 44.2 × 44.2 mm$^2$. Micro-CT scans were reconstructed using filtered back-projection at 28.5 $\mu$m isotropic voxel size with 1024 slices and image array of 1536 × 1536.

## 2.4 | Mechanical testing

After micro-CT imaging, cylindrical Tb cores of distal tibia were extracted for compressive mechanical testing and modulus measurement. Specimen preparation and mechanical testing were performed at the University of Iowa's Orthopaedic Biomechanics Laboratory. Details of specimen preparation and mechanical testing methods are described below.

### 2.4.1 | Specimen preparation

A cylindrical Tb core with a diameter of 8 mm was extracted from each distal tibia in situ along the central bone axis. A-P and M-L radiographs were used to determine the bone axis as well as to ensure removal of growth plate from the test specimens. Specimens were immersed in saline and cored using an 8.25 mm inner diameter diamond coring bit (Starlite Indus- tries, Rosemont, Pennsylvania). The core was separated from the inner radius by a razor saw, and the specimen ends were sanded smooth, flat, and parallel. Length and diameter of each specimen were measured three times using a micrometer and averaged, and extensometer attachment position was marked to be the middle 6 mm of the specimen length. Each core was wrapped in saline-soaked gauze, and frozen until thawed for testing. Minimum length of the specimens was 18 mm which satisfies the extensometer test criteria of minimum aspect ratio of 2:1 for Tb compression specimens and a 3:1 ratio for specimen length to extensometer gage length.[28]

### 2.4.2 | Mechanical testing

Mechanical testing of Tb cores was performed on an electromechanical materials testing machine (MTS
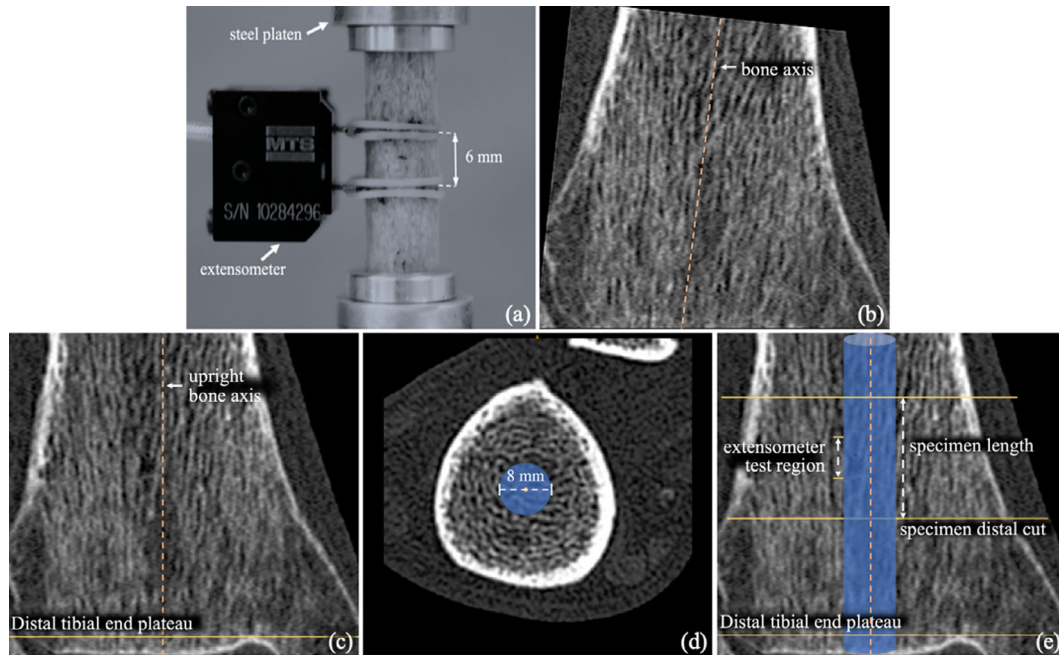
**FIGURE 1** Setup for axial compressive mechanical testing of a cylindrical Tb core using a 6-mm extensometer and matching VOI selection in CT scans. See the text for details

Insight, MTS Systems Corp., Eden Prairie, Minnesota). Each specimen core was placed between polished, unlubricated, plano-parallel steel platens for the compressive test. To reduce specimen end effects, strain was measured using a 6-mm gage length extensometer (model 632.29F-30, MTS Systems Corp., Eden Prairie, Minnesota) attached to the mid-section of the Tb core. A compressive preload of 10 N was applied at zero strain. Each specimen was preconditioned to a low strain at a strain rate of 0.005 s$^{-1}$, for at least 10 cycles and then loaded to failure. Finally, the 20% section of the stress–strain curve with the highest slope was used to determine modulus (MPa) of each Tb core. Our setup for mechanical testing with extensometer is shown in Figure 1a.

## 2.5 | Image preprocessing

Ankle CT images were rotated to align tibial bone axis with the coordinate $z$-axis to select upright volume of interests (VOI) for FEA and minimize errors related to inaccurate loading direction. Also, calcium hydroxyapatite (CHA) density (g/cc) at individual voxel was derived from CT intensity values using accompanied calibration phantom scans.

### 2.5.1 | Bone alignment and VOI selection

The tibial bone region including cortical and trabecular bone and the marrow space was segmented on CT
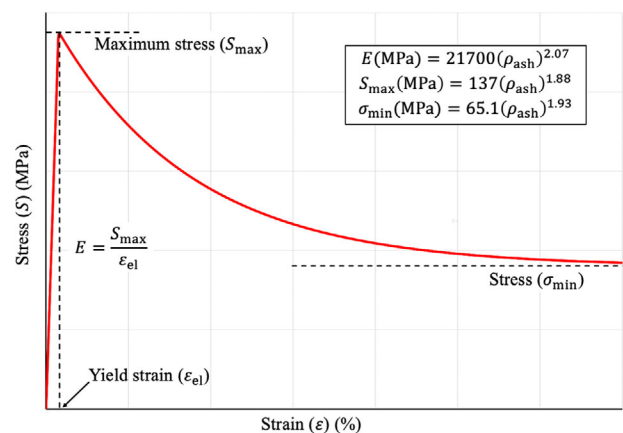


**FIGURE 2** Nonlinear stress–strain relationship for FEA. Voce isotropic hardening law was applied to model the nonlinear stress–strain relationship in the plastic phase beyond the point of yield strain $\varepsilon_{el}$ and maximum stress $S_{max}$

images using a previously validated automated algorithm involving soft thresholding, connectivity analysis, and morphological operations.[29] Forty percent axial peel was applied on the tibial bone region, and the peeled bone volume proximal to the site at 8% tibial length from the distal end plateau was used to compute the bone axis.[29] Forty percent axial peels were computed using in-plane distance transform[30,31] from the periosteal surface of the tibial bone and then thresholding to remove voxels with distance transform values lower than 40% of the highest distance transform values at individual axial slices. See Figure 2 in Li et al.[29] for further explanation.

Also, CT images were interpolated to 150-$\mu$m isotropic voxels using the windowed-sync method.[32] In human skeletons, Tb thickness values were observed to vary between 100 and 200 $\mu$m.[33] Therefore, the voxel size of 150 $\mu$m was selected toward the middle of the observed range of human Tb thickness values. It may be further clarified that, although the voxel size of 150 $\mu$m was used for image preprocessing and VOI selection, the optimum mesh element size for FEA was experimentally determined (see Sections 2.7 and 3). To reduce interpolation-related image resolution loss, the rotation for bone alignment and isotropic voxel interpolation steps were combined into one image transformation operation. As specified below, each VOI was chosen such that the cross-sectional diameter is always greater than the axial length to reduce microstructural disintegrity effects near the surface.[34]

For all experiments except for comparison with mechanical test results, upright cylindrical VOIs of diameter 8 mm and length 6.75 mm were selected after bone alignment. The VOI length of 6.75 mm was determined to approximately represent 2% of average human tibia length, and the diameter was set to be 8 mm to match the specimen diameter for mechanical testing. Each of these VOIs was located at 1.4 cm ($\sim$ 4% of an average tibial length) proximal to distal tibial end plateau with its axis matching with the tibial axis after bone alignment. Bone filling, alignment, and VOI selection were independently performed on individual repeat CT scans.

For the experiment comparing with mechanical test results, upright VOIs of diameter 8 mm and length 6 mm were used to match with the specimen core diameter and extensometer length shown in Figure 1b–e. First the original CT scan (b) was rotated to align bone axis with the image z-axis (c). An 8-mm circle was defined with its center at the center of gravity of the tibial bone region on the most proximal axial slice (d). An upright cylinder was constructed using the 8-mm circle. The section of the cylinder representing specimen core was identified using the reference of distal tibial end plateau and the position of the distal cut on the specimen core and specimen length recorded during mechanical experiments (e). Finally, the central 6-mm section of the cylinder representing the extensometer test region was selected as the VOI (e) for FEA.

## 2.5.2 | CT intensity to CHA density

Conversion of CT intensity numbers in Hounsfield unit (HU) to CHA density was performed in two steps— CT intensities to BMD (g/cc) and BMD to CHA density conversion. A Gammex RMI 467 Tissue Characterization Phantom (Gammex RMI, Middleton, Wisconsin) was used to calibrate CT HU numbers to BMD values.[20] The CHA density value $\rho_{CHA}(p)$ at a voxel $p$ was directly obtained from its BMD value $\rho_{BMD}(p)$ using known den-

sity values $D_{CHA}$ (3.18 g/cc) and $D_{water}$ (1 g/cc) and the following linear equation:

$$\rho_{CHA}(p) = \frac{(\rho_{BMD}(p) - D_{water})}{(D_{CHA} - D_{water})} \times D_{CHA}. \quad (1)$$

## 2.6 | Voxel-based continuum FE analysis

FEA is well established and widely used as a tool to quantitatively assess mechanical properties in various biomedical applications, especially those related to bone imaging.[35–37] Essentially, FEA simulates the physical phenomenon of a specific mechanical loading condition on a target object using a finite network of mesh elements. 3-D imaging is involved in FEA to define the geometry and material properties of mesh elements. Existing commercial software platforms are popularly used to solve FEA methods.[38,39] Primarily, different FEA methods vary in terms of their approaches in defining image-derived geometry and material properties of mesh elements, optimizing parametric environments of computational modeling, and biomedical applications revealing novel mechanical features using a target imaging modality with strong research and clinical significance. The computational platform and facilities provided within the ANSYS software (ANSYS Mechanical 2019 R2, Ansys Inc., Southpointe, Pennsylvania, USA) were used to implement our FEA methods. Thus, the FEA protocols and results presented in this paper may be easily adopted in future research and clinical studies.

A BMD-adjusted continuum FEA method was implemented on a voxel grid, where mesh elements were directly derived from isotropic voxel image. It may be clarified that no segmentation is involved in the meshing process and each voxel was added as a mesh element with its material property derived from its image intensity value. Specifically, each voxel was modeled using a cubic volume element with its center at the voxel coordinate location; also, 12 edge and eight vertex elements were added corresponding to the voxel edges and vertices. The connectivity between every pair of adjacent voxels or cubic elements was defined by specifying their common edges and vertices. Isotropic mechanical properties were assigned to individual voxel volume elements based on their CHA density values.

For nonlinear modeling of mechanical properties, the stress–strain relation was divided into two compartments characterizing the material behavior in elastic and plastic phases (Figure 2). Let $p_e$ denote the cubical volume element derived from an image voxel $p$. The ash density $\rho_{ash}(p)$ at the voxel $p$ and the elastic modulus $E(p_e)$, maximum stress $S_{max}(p_e)$, and saturation stress $\sigma_{min}(p_e)$ at the element $p_e$ are defined as follows:[40]

$$\rho_{ash}(p) = 0.0633 + 0.887\rho_{CHA}(p), \quad (2)$$

$$E(p_e) = 21700(\rho_{ash}(p))^{2.07}, \quad (3)$$

$$S_{max}(p_e) = 137(\rho_{ash}(p))^{1.88}, \quad (4)$$

$$\sigma_{min}(p_e) = 65.1(\rho_{ash})^{1.93}. \quad (5)$$

At an element $p_e$, the stress function $S_{p_e}(\varepsilon) \mid \varepsilon > \varepsilon_{el}(p_e)$ in the plastic phase beyond the yield strain $\varepsilon_{el}(p_e)$ was modeled using the Voce isotropic hardening law[41] as follows:

$$S_{p_e}(\varepsilon) = S_{max}(p_e) + R_1 \times \left(1 - e^{-b(\varepsilon - \varepsilon_{el}(p_e))}\right)$$
$$+ R_2 \times (\varepsilon - \varepsilon_{el}(p_e)) \mid \varepsilon \rangle \, \varepsilon_{el}(p_e), \quad (6)$$

where $R_1 = \sigma_{min}(p_e) - S_{max}(p_e)$, $R_2 = 0$, and $b = 10$.

In our experiments, FEA was applied to compute modulus within the elastic regime for the overall bone VOI. However, the applied strain on the top surface of the VOI is not uniformly distributed among individual FE elements. Therefore, several elements may enter the plastic phase, while the stress–strain values of the overall VOI still remain in the elastic regime. Within the ANSYS platform, Voce isotropic hardening is the sole option for modeling material property with a negative stress–strain slope in the plastic phase. The parameters of Voce isotropic hardening equation were optimized to resemble with the previously validated stress–strain curve by Keyak et al.[40] except that the nonlinear stress–strain relationship of the plastic phase was captured in a single equation of the Voce isotropic hardening law.

Moreover, two linear methods using different equations for elastic modulus were implemented within the same framework of voxel-based continuum FEA for CT imaging. The first linear continuum FEA method, referred to as linear FEA 1, used stress–strain relationship of Figure 2 without the plastic phase. The second method, referred to as linear FEA 2, used a linear stress–strain model, where the elastic modulus $E(p_e)$ of a voxel mesh element $p_e$ was defined using a different equation previously validated by Morgan et al.[42] To implement linear FEA 2, ash density was converted to apparent density by dividing with the previously reported ratio of 0.6 of the two density values.[43] For all linear and nonlinear methods, a Poisson's ratio of 0.3 was used, and boundary conditions were imposed to simulate a physical mechanical experiment of axial compressive loading. Specifically, the bottom surface of the cylindrical VOI was fixed in all coordinate directions, and a constant displacement along the z-direction was applied at every vertex element on the VOI top surface while restricting their movements in the x- and y-directions.

A Linux machine equipped with 64 GB RAM, 72 cores Intel(R) Xeon(R) Gold 6240 CPU at 2.60 GHz processor, and four Tesla V100-SXM2 GPUs with 32 GB memory each was used for computational FEA. The

3-D 8-Node structural solid element (SOLID185) within the ANSYS software was used to represent cubic mesh elements. Under the boundary conditions mentioned earlier, a total strain equivalent to 2% of the VOI core length was applied on all vertex elements at the top surface of the FE mesh, which was uniformly distributed over a predefined number of sub-steps. The average von Mises stress (MPa)[35] of volume elements observed on the top surface was computed using FEA to derive a stress–strain curve. Finally, the linear section of the stress–strain curve was experimentally determined, and the Tb modulus was computed as the stress–strain ratio at the maximum strain of the linear section. For the nonlinear FEA, a linear section was observed from 0% to 0.5% strain in the stress–strain relations of all the specimens. Based on these observations, 0.5% strain was used to compute the Tb modulus for both linear and nonlinear FEA methods. For the nonlinear method, Newton–Raphson's method was used for iterative convergence of force and displacement during each sub-step. Also, the ANSYS feature of NLGEOM was turned on to account for changes in elastic properties of individual elements during nonlinear shape deformation.

## 2.7 | Experiments and data analysis

Experiments were designed to optimize the sub-step numbers and mesh element size for the continuum FEA method using nonlinear modeling and evaluate the principle of the fundamental mechanics of structures in voxel-based continuum FEA of Tb microstructure from clinical CT imaging under a condition like in vivo imaging. Specifically, we examine the proportion of stress absorbed by Tb microstructure as compared to that by the marrow space. The performance of the voxel-based continuum FEA method using both linear and nonlinear models was evaluated in terms of—(1) CT repeat scan reproducibility, (2) correlation and agreement with micro-CT-derived modulus, and (3) correlation and agreement with experimentally measured modulus.

Reference values of the Tb modulus measure were computed using micro-CT imaging at 28.5 $\mu$m isotropic voxel resolution. First, the micro-CT scan was semi-automatically registered to the corresponding CT image after bone alignment at the upright position (Section 2.5.1), while preserving the original micro-CT resolution. ITK-SNAP software and its graphical user interface (Kitware Inc., Carrboro, North Carolina) was used for image registration. A previously validated FEA method[10] was applied on registered micro-CT data over the matching upright VOI after binary segmentation of bone and nonbone voxels. Manual thresholding and connectivity analysis were used to segment bone and nonbone voxels. Specifically, two mutually blinded observers selected threshold values for each micro-CT image, and the average of two selected values was used for

thresholding the specific image. Finally, each Tb voxel was modeled by a cubical mesh element of 28.5-$\mu$m isotropic size, and a homogenous isotropic elastic tissue property with modulus of 10 GPa and Poisson's ratio of 0.3 was assigned to each mesh element.[10]

To optimize the ANSYS parameters, the relative modulus of a specimen at a given parameter combination was computed as the percent of the highest modulus value obtained among all parameter combinations, and the convergence criterion was defined at 100% relative modulus for all specimens. First, the sub-step parameter was optimized among 10 different sub-step numbers of 5, 10, 20, 30, 40, 50, 100, 150, 200, 250, and the default force and displacement tolerance parameters.[1] Subsequently, the force tolerance parameter was determined among the values of 0.05%, 0.1%, 0.5%, 1% with the optimum sub-step parameter and the default value for the displacement parameter. Finally, the displacement tolerance parameter was determined among the values of 0.5%, 1%, 5%, 10% with optimum parameters for sub-step number and force.

To examine the sensitivity of mesh element size and optimize it, CT scans were resampled at 75, 100, 150, 200, 250, 300, 400, 500, 600, 700, 800, 900, and 1000 $\mu$m isotropic voxels, and FE meshes were constructed at different element sizes. Nonlinear continuum FEA was performed over matching VOIs at different element sizes using the optimum ANSYS setup parameters. At each element size, mean and standard deviation (std) of computed modulus values and their Pearson correlation with micro-CT-derived reference values were computed. The mesh element size with the highest correlation with micro-CT-derived values was selected as the optimum mesh element size, and all subsequent experiments were performed using the optimum ANSYS parameters and mesh element size.

The intra-class correlation (ICC) of computed modulus values was computed to examine repeat scan reproducibility of different CT-based FEA. Pearson correlation of CT-derived FEA modulus values with micro-CT-derived reference values and mechanical test results was computed to examine the performance of different CT-based FEA methods to provide surrogate modulus measures of Tb microstructure. Agreements of CT-based modulus values with micro-CT and mechanical test derived measures were examined in terms of concordance correlation coefficient (CCC), and mean(std) of modulus values using different methods are reported. Finally, CT- and micro-CT-derived Tb bone microstructural measures (Table 1) over matching upright VOIs of diameter 8 mm and length 6.75 mm were compared, and the values are presented to facilitate the discussions related to comparison between CT- and micro-CT-derived FEA results.

---

[1] ANSYS default values for the sub-step number and tolerance for force and displacement convergence are 10, 0.5%, and 5%, respectively.

**TABLE 1** List of CT-derived Tb measures: The nomenclature of Tb measures used by Bouxsein et al.[52] and Chen et al.[20] is followed here

| Tb measure (unit) | Description |
|---|---|
| Tb.BVF(%) | Tb volume fraction |
| Tb.NA(1/mm) | Tb network area density, i.e. the average area of the medial surface of segmented bone per unit VOI |
| Tb.Th($\mu$m) | Mean Tb thickness computed using star-line and fuzzy distance analysis[53] |
| Tb.Sp($\mu$m) | Mean Tb spacing, i.e. the space between trabecular microstructures computed using star-line and fuzzy distance analysis[53] |

Tb, trabecular bone.

## 3 | RESULTS AND DISCUSSION

Matching axial slices from CT and micro-CT scans are shown in Figure 3. Although matching Tb microstructures are visible in CT and micro-CT scans, they appear fuzzily in CT scans and binary segmentation of these trabeculae is prone to errors. Such segmentation errors in CT scans add artifactual micro-network discontinuities failing computational stress propagation in FEA that causes significant FEA errors. The results of the sub-step selection experiment are presented in Figure 4 that shows the mean and std of relative modulus at different values of sub-step parameter ($n = 24$). At lower values of the parameter, instability in computed modulus was observed causing less than 100% relative modulus and high std among specimens. As the sub-step number was increased, the mean relative modulus moved toward 100%, and the std was reduced. Hundred percent relative modulus was achieved for all specimens at sub-step numbers $\geq 50$. Also, it was observed that instability in computed modulus values was reduced by reducing the parameters for force and displacement tolerance, and the 100% percent relative modulus was achieved for all specimens at 0.5% and 5% values for force and displacement parameters, respectively (results not presented). Based on the results of these optimization experiments, the following parameter setup was selected and applied for all evaluative experiments— sub-step number: 50; force tolerance: 0.5%; displacement tolerance: 5%.

Results of sensitivity analysis with mesh element size are shown in Figure 5. Pearson correlation coefficients ($r$-values) of CT-based nonlinear FEA-derived modulus values with micro-CT-derived reference values at varying mesh element size are shown in Figure a. Highest correlation of 0.90 was observed at 100 $\mu$m isotropic voxel element size. High computational complexity prohibited testing FEA performance at voxel mesh element size below 75 $\mu$m. Due to the lack of data points on FEA
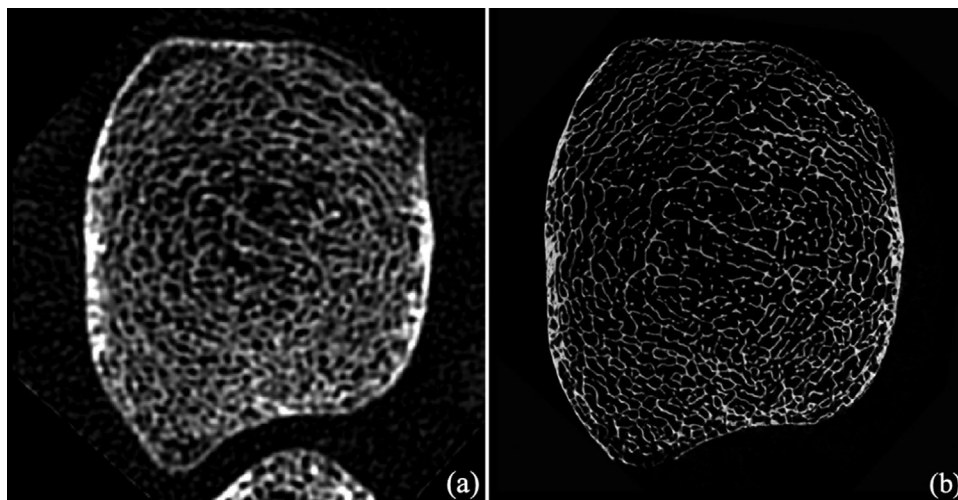
**FIGURE 3**    Matching axial slices from CT (a) and micro-CT (b) scans of the same specimen
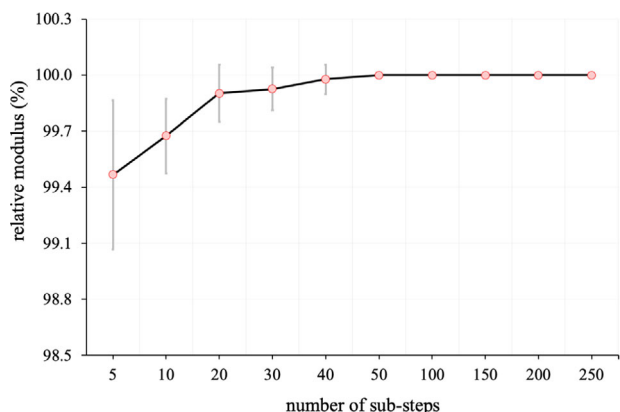


**FIGURE 4**    Optimization of the sub-step parameter for nonlinear continuum FEA. Relative modulus of a specimen at a given parameter was defined as the percent of the maximum modulus value obtained for that specimen among all parameter values. Mean and std of relative modulus values of all specimens are shown as a function of sub-step number. At the sub-step number of 50 and higher, 100% relative modulus values were observed for all specimens with std of "0"

performance at element sizes below 75 $\mu$m, it was difficult to confirm whether a plateau of FEA performance was formed at 100 $\mu$m element size. However, a monotonic decrease in FEA performance was observed at higher mesh element size beyond 100 $\mu$m. Based on the observations that the FEA performance was not improved at 75-$\mu$m element size with higher computational complexity and that the performance monotonically decreased at element sizes higher than 100 $\mu$m up to 400 $\mu$m, 100-$\mu$m isotropic voxel was chosen as the optimum FE mesh element. Mean and std of modulus values are displayed as functions of mesh element size in Figure b. Monotonic increase in mean values of the computed modulus was observed for mesh element size up to 800 $\mu$m, which was followed by a decline in mean values. Changes in computed modulus values with mesh element size are governed by two different phenomena—(a) changes in percent of effective elements in plastic phase at different mesh element sizes and (b) nonlinearity of elastic property of individual elements with ash density. It was found from our
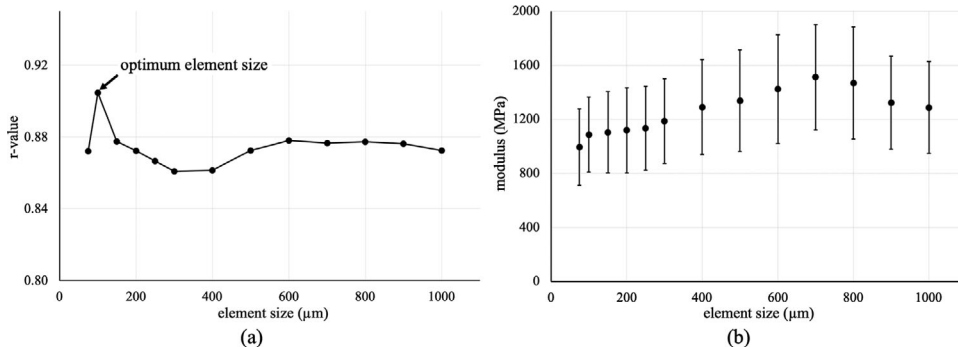


**FIGURE 5**    Sensitivity of mesh element size in voxel-based nonlinear continuum FEA. (a) Pearson correlation of CT-derived modulus values with micro-CT-derived reference values as a function of mesh element size. (b) Mean and std of computed modulus values at different element sizes

experimental results that CHA weighted fraction of elements in plastic phase decreased with increasing element size, which positively contributed to the computed modulus values with increasing element size. Again, with increasing element size, the fixed amount of bone material is distributed over a larger volume reducing density of bone elements linearly proportionate to the increasing volume. On the other hand, following Equation 3, the modulus of an element changes as a higher order polynomial function. These two factors together cause negative contribution to computed modulus with increasing element size. The nonmonotonic behavior of mean modulus values with increasing mesh element size may be explained by the above two different phenomena with opposite effects on computed modulus values. Specifically, the inflection point on the modulus versus element size curve (see Figure 5b) occurs when the influence of one phenomenon exceeds that of the other.

The results of application of nonlinear continuum FEA on one CT cadaveric ankle scan are illustrated in Figure 6, and the selected VOI is shown in (a). Mean(std) of tibial diameter of 33.3(1.8) mm was observed at 6% distal site among all specimens ($n = 24$). In other words, the VOI represents the central 24.2% of the tibial bone at 6% tibial length proximal to the distal end plateau. For CT-based FEA experiments, the average number of vertex elements of 5 065 and voxel volume elements of 4 987 were observed on the top surface, which were used for applying strain and measuring stress, respectively (see Figure 6b). On an average, 355K vertex, 105K edge, and 344K volume elements were observed over a VOI, and mean(std) of computed modulus values were 1084.3(445.4) MPa with [min max] as [256 1872] MPa. Runtime for CT-based FEA on a VOI core was 13.6(3.5) min running on a GPU equipped desktop (see Section 2.6).

Color-coded volume rendition of matching VOIs from CT and micro-CT scans of a specimen is shown in Figure 6c and d, respectively. CT- and micro-CT-derived modulus values of the specimen were 1025 and 1458 MPa, respectively. FEA-derived von Mises stress over the target VOI of (c) and (d) are illustrated in (e) and (f), respectively. Agreements between Tb microstructures and the high stress regions are visible for both CT and micro-CT VOIs. The results of quantitative experiments evaluating the agreement between Tb microstructure and high stress region for CT-based nonlinear continuum FEA are presented in Figure 7. Figure 7a presents the distribution of von Mises stress at different CHA density; maximum stress (see Equation 4) at different CHA density is also shown. It is worth mentioning that the maximum stress line defines the upper limit of the von Mises stress experienced at a given CHA value. Also, nonlinearity between CHA density and stress is observed in both maximum stress line and the general trend of stress-CHA density distri-

bution. Figure b shows the normalized stress histogram over segmented Tb microstructure and marrow regions among all specimens ($n = 24$). A previously validated automated method by Chen et al.[44] was used to segment the Tb and marrow regions. Also, it may be clarified that segmentation of bone and marrow regions was used only for validation experiments, and no separation was needed for linear or nonlinear continuum FEA methods. Stress histograms were normalized by setting the area under the curve to '1' for better visual representation. Stress histogram from marrow space (green) falls rapidly with increasing stress and reaches to '0' at stress $\geq$ 16.1 MPa. More importantly, the mean of the upper three percentile of stress values within marrow voxels excluding those adjacent to segmented Tb voxels was 3.7 MPa. Note that marrow voxels adjacent to Tb voxels fractionally occupy bone material at in vivo resolution, and therefore associated with relatively higher FE stress values. On the other hand, the histogram over Tb microstructure shows higher stress values, and the peak is observed at 14.7 MPa. Mean(std) of observed stress values over Tb microstructure and marrow regions were 16.4(8.1) and 3.1(4.0) MPa, respectively, and an unpaired $t$ test confirmed significance ($p < 10^{-8}$) of the difference in stress distribution over the two regions. For linear FEA 1, mean(std) of the stress values over Tb microstructure and marrow regions were 16.8(8.2) and 3.2(4.3) MPa ($p < 10^{-8}$), while the values for linear FEA 2 were 19.1(7.6) and 4.9(5.3) MPa ($p < 10^{-9}$), respectively. These observations confirm that CT-based continuum FEA under a condition like in vivo imaging complies with the basic principle of structural mechanics that majority of stress is absorbed by Tb microstructure as compared with the marrow space without requiring binary segmentation of Tb and marrow regions. This relaxation of binary segmentation creates opportunities of applying FEA and analysis of mechanical properties at relatively low-resolution in vivo CT imaging, while accounting for spatial microdistribution of bone and estimating its impact on bone modulus.

High-repeat CT scan reproducibility ($n = 24$) was observed for computed modulus values using all three continuum FEA methods. Specifically, the observed ICC values of repeat scan reproducibility of modulus computation using nonlinear and linear FEA 1 and 2 methods were 0.98, 0.98, and 0.98, respectively. It is worth mentioning that individual repeat scans were processed independently. Thus, the observed results represent the reproducibility of the entire process including positioning and CT imaging, bone filling and alignment, and voxel-based continuum FEA. Comparative results of Tb modulus values obtained using CT- and micro-CT-based FEA and mechanical testing methods are summarized in Table 2. CT-based modulus values using nonlinear FEA and the micro-CT-derived gold-standard values of modulus are plotted in Figure 8a ($n = 13$). No visually obvious outlier was observed in this plot, and
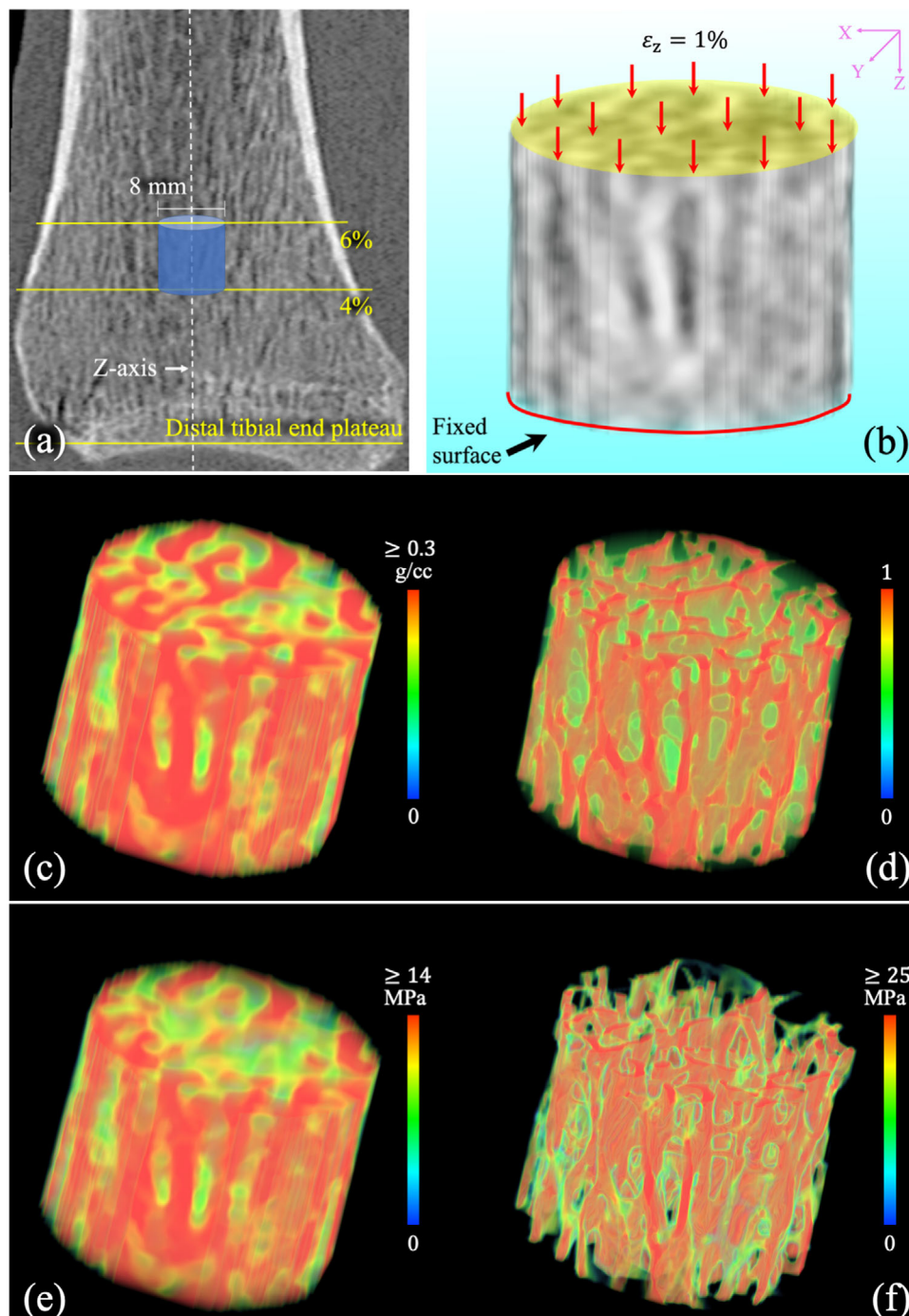
**FIGURE 6** CT-based nonlinear continuum FEA and computation of Tb microstructural modulus. (a) Overlay of the cylindrical VOI (in blue) for FEA on the sagittal image slice from a distal tibia CT scan. (b) FEA boundary condition and loading protocol on the extracted Tb core. (c) Color-coded volume rendition of the normalized CHA density map over the VOI of (b). (d) Color-coded volume rendition of the matching micro-CT VOI of (b). (e,f) Same as (c,d) but for FEA recorded von Mises stress over CT (e) and micro-CT (f) VOIs, respectively

similar plots (not presented) were found for the two continuum FEA-based linear methods. High linear correlation between CT- and micro-CT-based modulus values endorses the agreement of stress-flow continuity along Tb microstructure using CT-based continuum FEA at a condition similar to in vivo imaging without explicit Tb micro-segmentation and that using micro-CT with binary segmentation of Tb microstructure. However, mean(std)

of CT-derived modulus values were significantly different from the micro-CT-derived values with low CCC values over the range [0.24 0.43] (see Table 2a). Similar correlation results, presented in Table 2b, were observed between CT-based modulus values and those obtained by mechanical testing. Modulus values obtained using CT-based nonlinear FEA and mechanical testing are plotted in Figure 8b ($n = 21$). Three
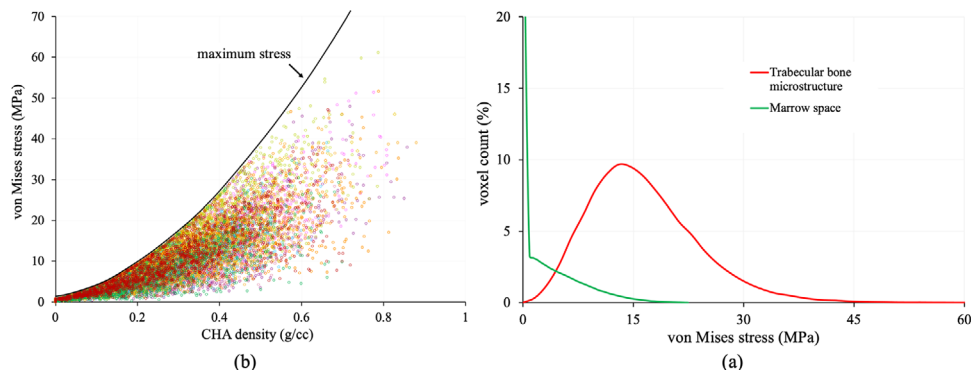
**FIGURE 7**    Nonlinear FE stress distribution at different CHA densities and over Tb microstructure and marrow space. (a) Computed von Mises stress distribution at different CHA densities. Different colors are used for observations from different specimens. The maximum stress corresponding to yield stress is shown as a function of CHA density. The nonlinearity between von Mises stress and CHA density is visually apparent. (b) Stress histogram over segmented Tb microstructure and marrow regions

**TABLE 2**    Results of Pearson and concordance correlation analysis of different CT-based FEA computed modulus values with micro-CT-derived reference values and experimental modulus from mechanical test. (a) Comparison with micro-CT measures. (b) Comparison with experimental measures

| (a) | | | | (b) | | | |
|---|---|---|---|---|---|---|---|
| Methods | Mean(std) | Correlation (r)* | CCC | Methods | Mean(std) | Correlation (r)* | CCC |
| Micro-CT | 1498.9(103.6) | – | – | Mechanical Test | 1748.7(391.5) | – | – |
| Nonlinear FEA | 1087.2(276.9) | 0.90 | 0.20 | Nonlinear FEA | 1282.9(437.9) | 0.87 | 0.53 |
| Linear FEA 1[40] | 1044.7(289.2) | 0.87 | 0.24 | Linear FEA 1[40] | 1282.8(426.1) | 0.80 | 0.48 |
| Linear FEA 2[42] | 1411.3(308.6) | 0.88 | 0.43 | Linear FEA 2[42] | 1636.7(417.0) | 0.82 | 0.79 |

Linear FEA 1 refers to the method using stress–strain relationship of Figure 2 without the plastic phase.[40]
Linear FEA 2 refers to the method using the elastic modulus $E(\cdot)$ defined using a validated equation by Morgan et al.[42]
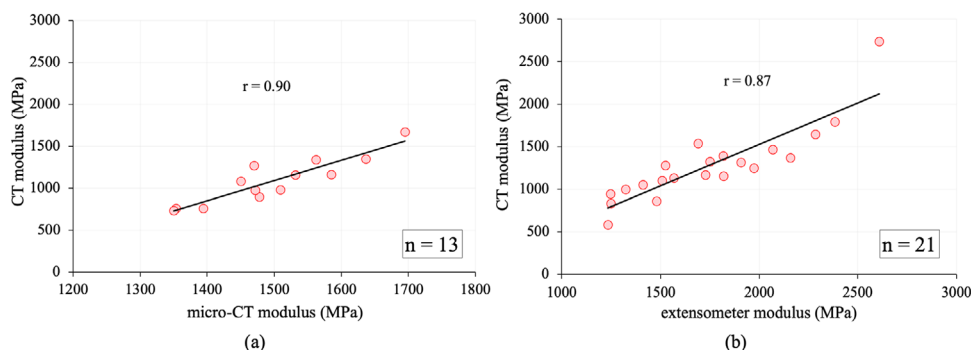*Pearson linear correlation analysis was used.



**FIGURE 8**    Comparison among Tb modulus measures using CT, micro-CT, and mechanical testing. (a,b) Linear correlation (r value) of CT-derived modulus values using a nonlinear continuum FEA with micro-CT-derived (a) and experimentally measured (b) reference modulus values

specimens were excluded for this analysis due to failure during mechanical testing. Mean(std) of CT-based modulus values were 1087.2(276.9) and 1282.9(437.9) MPa for Figure 8a and b, respectively. It may be noted that the sample VOIs for (a) were selected at approximately 4% distal tibial site representing nearly 2% of tibial length. On the other hand, the VOIs for (b) were defined by position of the distal cut on the specimen core and specimen length recorded during mechanical experiments.

Observed differences in mean CT modulus values may be explained by the differences in VOI selection protocols for experiments presented in (a) and (b).

Comparative results between CT- and micro-CT-derived values of different Tb microstructural measures (Table 1) are presented in Table 3. Means of CT-derived values of Tb.BVF, Tb.NA, and Tb.Th measures were significantly lower (CCC $\in$ [0.06 0.21]) than micro-CT-derived values, while the mean of CT values of Tb.Sp

**TABLE 3** Summary statistics and Pearson and concordance correlation analysis of different Tb microstructural measures derived from CT and micro-CT images. See Table 1 for the definitions of Tb measures

| Tb measure | CT | micro-CT | r value | CCC |
|---|---|---|---|---|
| Tb.BVF(%) | 13.4(3.7) | 26.6(1.9) | 0.82 | 0.06 |
| Tb.NA(1/mm) | 0.5(0.1) | 0.8(0.2) | 0.79 | 0.20 |
| Tb.Th($\mu$m) | 260.3(32.2) | 223.2(22.2) | 0.43 | 0.21 |
| Tb.Sp($\mu$m) | 584.2(149.4) | 473.0(55.9) | −0.70 | 0.32 |

were higher (CCC = 0.32) than its micro-CT values. However, CT-derived values of all Tb measures except Tb.Th showed strong linear correlation ($r \geq 0.70$) with their micro-CT-derived reference values.

High linear correlation of CT-derived modulus values using continuum FEA methods with micro-CT and mechanical testing derived reference values suggests that the CT-based continuum FEA is useful to obtain a surrogate modulus measure of Tb microstructure. Moreover, the CT images used in this study were acquired under a condition similar to in vivo imaging using a CT protocol previously applied on human studies.[27,45] Therefore, our experiments and results also validate continuum FEA methods for computing surrogate measures of Tb microstructural modulus using in vivo CT imaging of peripheral sites suitable for human studies. Large deviation in CT-derived modulus values as compared to micro-CT or mechanical test-derived results was observed, which suggests that CT-derived modulus values may not be used as actual modulus measures. Also, our observations on CT-based computation of Tb microstructural modulus are consistent with our findings related to CT- and micro-CT-derived values of Tb microstructural metrics and those reported in literature.[20,46,47] Finally, it may be clarified that, since the $r$ values ($\in [0.87\ 0.90]$) are high, it is always possible to use the corresponding regression equation to estimate the reference modulus values from CT-based FEA-derived values.

The nonlinear FEA method resulted the maximum deviation from micro-CT-derived values with the lowest CCC of 0.20. Linear FEA 2 produced higher mean modulus value than the micro-CT-derived value, while the other linear method generated lower mean value. Also, it is worth highlighting that, although, linear FEA-based modulus values were closer to their reference values, their accuracies or CCCs were low except for the comparison of linear FEA 2 with mechanical test measures (CCC = 0.79). Also, for nonlinear FEA at 0.5% strain it was observed that on average 39.4% voxels remain in the elastic phase while 60.6% voxels enter the plastic phase after simulation. These results suggest that the nonlinear component of the plastic phase is one factor behind lower values of nonlinear FEA modulus as compared to their reference values. Also, it may be empha-

sized that limited signal-to-noise ratio and spatial resolution of in vivo imaging add various artifacts including noise, partial voluming, structure blurring, loss of thinner trabeculae etc. High Pearson correlation of continuum FEA with both micro-CT and mechanical test-derived reference values suggests that the continuum modeling approach is suitable in mitigating the effect of stress-flow along Tb microstructure at the limited regime of in vivo imaging in the presence of noise and other artifacts.

There are some limitations in this study that should be clarified. The data presented here were based on in vitro cadaveric specimens, which are the closest to in vivo imaging conditions. However, there are inherent differences between in vitro cadaveric and in vivo human experiments, which may not be quantified.[48] The primary difference is the lack of movement artifacts in CT scans of cadaveric specimens; however, the motion artifacts are minimal for high-speed CT imaging used here, which takes only 23.2 s to acquire a 10-cm long scan of the tibia. Also, no motion artifact was observed in our recent studies involving in vivo CT scans of human subjects using similar protocols.[20,27,49,50] Another limitation of this study was that parallel platens testing was used to experimentally measure actual compressive modulus of Tb cores. It has been previously demonstrated that platens compression testing underestimates Tb modulus measures.[51] Also, it may be clarified that relatively high-resolution CT imaging with 0.3 mm $z$-resolution was used for all our experiments, and similar performance of CT-based FEA on Tb microstructure may not be obtained using low-resolution scans. However, it is also worth mentioning that all frontline CT scanners from different vendors can produce images at higher resolution than the scanner used in the current paper.

In summary, voxel-based continuum FEA provides effective surrogate measures of Tb microstructural modulus from peripheral CT imaging at in vivo condition that highly correlates with its reference measure, while the actual values are significantly different. Linear correlation of computed modulus using linear model-based continuum FEA with reference modulus values is comparable to that obtained using nonlinear modeling. Also, linear FEA-derived modulus values were closer to the micro-CT and experimentally derived reference values than the more complex nonlinear FE model with plasticity. Thus, a more complex model with nonlinear plasticity did not yield better results in terms of closeness of CT-derived values to the micro-CT and experimentally derived reference values. Among the two linear methods, the CT-based linear continuum FEA modeling proposed by Morgan et al.[42] showed better performance. It may be clarified that our experimental setup was designed to evaluate the Tb modulus measure, which has been previously shown to highly correlate with bone strength.[26] Thus, in vivo CT-based FEA, evaluated in the current paper, may be useful in human

studies exploring impacts of diseases or therapeutic interventions on bone microstructural fragility.

# 4 | CONCLUSION

This paper demonstrates the application of clinical CT-based continuum FEA under a condition similar to in vivo imaging to compute mechanical properties of Tb microstructure that directly operates on CT-derived BMD images without requiring any segmentation of Tb and marrow regions, while accounting for bone material distribution at microstructural level. Our experimental results demonstrate that voxel-based continuum FEA at clinical CT imaging under a condition similar to in vivo imaging complies with the fundamental mechanics of structures that stresses follow the Tb microstructure and stress leakages in the marrow region is nominal, which has been previously shown at high resolution ex vitro imaging. Experimental results demonstrate that CT-based continuum FEA is repeat scan reproducible, and computed values of the modulus measure correlate with its values obtained using micro-CT and mechanical testing. In other words, CT-based continuum FEA provides an effective surrogate measure of Tb microstructural modulus and alleviates the requirement of Tb micro-network segmentation, while accounting for bone material distribution at microstructural level. This relaxation of Tb microstructural segmentation will extend the scope of FEA application to relatively low-resolution imaging often available in routine clinical scans, while capturing spatial nonuniformity of bone micro-distribution.

## CONFLICT OF INTEREST STATEMENT
The authors have no conflicts to disclose.

## REFERENCES

1. Riggs BL, Khosla S. Better tools for assessing osteoporosis. *J Clin Invest*. 2012; 122: 4323-4324.
2. Sözen T, Özışık L, Başaran NÇ. An overview and management of osteoporosis. *Eur J Rheumatol*. 2017; 4: 46-56.
3. Melton LJ 3rd, Kan SH, Wahner HW, Riggs BL. Lifetime fracture risk: an approach to hip fracture risk assessment based on bone mineral density and age. *J Clin Epidemiol*. 1988; 41: 985-994.
4. Legrand E, Audran M, Guggenbuhl P, et al. Trabecular bone microarchitecture is related to the number of risk factors and etiology in osteoporotic men. *Microsc Res Tech*. 2007; 70: 952-959.
5. Parfitt AM, Mathews CHE, Villanueva AR, Kleerekoper M, Frame B, Rao DS. Relationships between surface, volume, and thickness of iliac trabecular bone in aging and in osteoporosis - implications for the microanatomic and cellular mechanisms of bone loss. *J Clin Invest*. 1983; 72: 1396-1409.
6. Sornay-Rendu E, Boutroy S, Duboeuf F, Chapurlat RD. Bone microarchitecture assessed by HR-pQCT as predictor of fracture risk in postmenopausal women: the OFELY study. *J Bone Miner Res*. 2017; 32: 1243-1251.
7. Litwic A, Westbury L, Carter S, Ward K, Cooper C, Dennison E. Self-perceived fracture risk in the global longitudinal study of osteoporosis in women: its correlates and relationship with bone microarchitecture. *Calcif Tissue Int*. 2020; 106: 625-636.
8. Rajapakse CS, Leonard MB, Bhagat YA, Sun W, Magland JF, Wehrli FW. Micro–MR imaging–based computational biomechanics demonstrates reduction in cortical and trabecular bone strength after renal transplantation. *Radiology*. 2012; 262: 912-920.
9. Rajapakse CS, Magland JF, Wald MJ, et al. Computational biomechanics of the distal tibia from high-resolution MR and micro-CT images. *Bone*. 2010; 47: 556-563.
10. Ulrich D, van Rietbergen B, Weinans H, Rüegsegger P. Finite element analysis of trabecular bone structure: a comparison of image-based meshing techniques. *J Biomech*. 1998; 31: 1187-1192.
11. Van Ruijven L, Mulder L, Van Eijden T. Variations in mineralization affect the stress and strain distributions in cortical and trabecular bone. *J Biomech*. 2007; 40: 1211-1218.
12. Keyak J, Sigurdsson S, Karlsdottir G, et al. Effect of finite element model loading condition on fracture risk assessment in men and women: the AGES-Reykjavik study. *Bone*. 2013; 57: 18-29.
13. Keyak JH, Kaneko TS, Tehranzadeh J, Skinner HB. Predicting proximal femoral strength using structural engineering models. *Clin Orthop Relat Res*. 2005; 437: 219-228.
14. Chevalier Y, Pahr D, Allmer H, Charlebois M, Zysset P. Validation of a voxel-based FE method for prediction of the uniaxial apparent modulus of human trabecular bone using macroscopic mechanical tests and nanoindentation. *J Biomech*. 2007; 40: 3333-3340.
15. Van Rietbergen B, Majumdar S, Newitt D, MacDonald B. High-resolution MRI and micro-FE for the evaluation of changes in bone mechanical properties during longitudinal clinical trials: application to calcaneal bone in postmenopausal women after one year of idoxifene treatment. *Clin Biomech*. 2002; 17: 81-88.
16. Graeff C, Timm W, Nickelsen TN, et al. Monitoring teriparatide-associated changes in vertebral microstructure by high-resolution CT in vivo: results from the EUROFORS study. *J Bone Miner Res*. 2007; 22: 1426-1433.
17. Wehrli FW, Ladinsky GA, Jones C, et al. In vivo magnetic resonance detects rapid remodeling changes in the topology of the trabecular bone network after menopause and the protective effect of estradiol. *J Bone Miner Res*. 2008; 23: 730-740.
18. Pistoia W, Rietbergen Bv, Lochmüller EM, Lill AC, Eckstein F, Rüegsegger P. Estimation of distal radius failure load with micro-finite element analysis models based on three-dimensional peripheral quantitative computed tomography images. *Bone*. 2002; 30: 842-848.
19. Wehrli FW, Rajapakse CS, Magland JF, Snyder PJ. Mechanical implications of estrogen supplementation in early postmenopausal women. *J Bone Miner Res*. 2010; 25: 1406-1414.
20. Chen C, Zhang X, Guo J, et al. Quantitative imaging of peripheral trabecular bone microarchitecture using MDCT. *Med Phys*. 2018; 45: 236-249.
21. Liebl H, Garcia EG, Holzner F, et al. In-vivo assessment of femoral bone strength using Finite Element Analysis (FEA) based on routine MDCT imaging: a preliminary study on patients with vertebral fractures. *PLoS One*. 2015; 10: 1-15.
22. Rayudu NM, Anitha DP, Mei K, et al. Low-dose and sparse sampling MDCT-based femoral bone strength prediction using finite element analysis. *Arch Osteoporos*. 2020; 15: 1-9.
23. Bauer JS, Sidorenko I, Mueller D, et al. Prediction of bone strength by $\mu$CT and MDCT-based finite-element-models: how much spatial resolution is needed? *Eur J Radiol*. 2014; 83: 36-42.

24. Zhao S, Arnold M, Ma S, et al. Standardizing compression testing for measuring the stiffness of human bone. *Bone Joint Res*. 2018; 7: 524-538.

25. Schaffler MB, Burr DB. Stiffness of compact bone: effects of porosity and density. *J Biomech*. 1988; 21: 13-16.

26. Fyhrie DP, Vashishth D. Bone stiffness predicts strength similarly for human vertebral cancellous bone in compression and for cortical bone in tension. *Bone*. 2000; 26: 169-173.

27. Zhang X, Comellas AP, Regan EA, et al. Quantitative CT-based methods for bone microstructural measures and their relationships with vertebral fractures in a pilot study on smokers. *JBMR Plus*. 2021; 5: 1-14.

28. Keaveny TM, Borchers RE, Gibson LJ, Hayes WC. Trabecular bone modulus and strength can depend on specimen geometry. *J Biomech*. 1993; 26: 991-1000.

29. Li C, Jin D, Chen C, et al. Automated cortical bone segmentation for multirow-detector CT imaging with validation and application to human studies. *Med Phys*. 2015; 42: 4553-4565.

30. Borgefors G. Distance transformations in digital images. *Comput Vision Graph Image Process*. 1986; 34: 344-371.

31. Saha PK, Strand R, Borgefors G. Digital topology and geometry in medical imaging: a survey. *IEEE Trans Med Imaging*. 2015; 34: 1940-1964.

32. Meijering EH, Niessen WJ, Pluim JP, Viergever MA, "Quantitative comparison of sinc-approximating kernels for medical image interpolation," Proceedings of *International Conference on Medical Image Computing and Computer-Assisted Intervention*, 210-217, 1999.

33. Ding M, Hvid I. Quantification of age-related changes in the structure model type and trabecular thickness of human tibial cancellous bone. *Bone*. 2000; 26: 291-295.

34. Linde F, Hvid I, Madsen F. The effect of specimen geometry on the mechanical behaviour of trabecular bone specimens. *J Biomech*. 1992; 25: 359-368.

35. Logan DL. *A First Course in the Finite Element Method*. Cengage Learning; 2011.

36. Keyak J, Rossi S, Jones K, Les C, Skinner H. Prediction of fracture location in the proximal femur using finite element models. *Med Eng Phys*. 2001; 23: 657-664.

37. Crawford RP, Cann CE, Keaveny TM. Finite element models predict in vitro vertebral body compressive strength better than quantitative computed tomography. *Bone*. 2003; 33: 744-750.

38. Madenci E, Guven I. *The Finite Element Method and Applications in Engineering Using ANSYS*. Springer; 2015.

39. Barbero EJ. *Finite element analysis of composite materials using Abaqus™*. CRC press; 2013.

40. Keyak J, Lee I, Nath D, Skinner H. Postfailure compressive behavior of tibial trabecular bone in three anatomic directions. *J Biomed Mater Res*. 1996; 31: 373-378.

41. Voce E. A practical strain hardening function. *Metallurgia*. 1955; 51: 219-226.

42. Morgan EF, Bayraktar HH, Keaveny TM. Trabecular bone modulus–density relationships depend on anatomic site. *J Biomech*. 2003; 36: 897-904.

43. Schileo E, Taddei F, Malandrino A, Cristofolini L, Viceconti M. Subject-specific finite element models can accurately predict strain levels in long bones. *J Biomech*. 2007; 40: 2982-2989.

44. Chen C, Jin D, Zhang X, Levy SM, Saha PK, Segmentation of trabecular bone for in vivo CT imaging using a novel approach of computing spatial variation in bone and marrow intensities. *Proceedings of Asian Conference on Computer Vision*, 3-15, 2016.

45. Janz KF, Burns TL, Levy SM. Tracking of activity and sedentary behaviors in childhood: the iowa bone development study. *Am J Prev Med*. 2005; 29: 171-178.

46. Guha I, Klintström B, Klintström E, et al. A comparative study of trabecular bone micro-structural measurements using different CT modalities. *Phys Med Biol*. 2020; 65: 1-14.

47. Link TM. Osteoporosis imaging: state of the art and advanced imaging. *Radiology*. 2012; 263: 3-17.

48. MacNeil JA, Boyd SK. Accuracy of high-resolution peripheral quantitative computed tomography for measurement of bone quality. *Med Eng Phys*. 2007; 29: 1096-1105.

49. Saha PK, Oweis RR, Zhang X, et al. Effects of fluoride intake on cortical and trabecular bone microstructure at early adulthood using multi-row detector computed tomography (MDCT). *Bone*. 2021; 146: 1-11.

50. Saha PK, Liu Y, Chen C, et al. Characterization of trabecular bone plate-rod microarchitecture using multirow detector CT and the tensor scale: algorithms, validation, and applications to pilot human studies. *Med Phys*. 2015; 42: 5410-5425.

51. Keaveny TM, Pinilla TP, Crawford RP, Kopperdahl DL, Lou A. Systematic and random errors in compression testing of trabecular bone. *J Orthop Res*. 1997; 15: 101-110.

52. Bouxsein ML, Boyd SK, Christiansen BA, Guldberg RE, Jepsen KJ, Muller R. Guidelines for assessment of bone microstructure in rodents using micro-computed tomography. *J Bone Miner Res*. 2010; 25: 1468-1486.

53. Liu Y, Jin D, Li C, et al. A robust algorithm for thickness computation at low resolution and its application to in vivo trabecular bone CT imaging. *IEEE Trans Biomed Eng*. 2014; 61: 2057-2069.